Mesosphere and Lower Thermosphere changes caused by the July 2, 2019 total Eclipse in South America over the Andes Lidar Observatory, Cerro Pachon, Chile.

F. Vargas[1], A. Liu[2], G. Swenson[1], Segura, C.[3], P. Vega[4], J. Fuentes[5], D. Pautet[6], M. Taylor[6], Y. Zhao[6], Y. Morton[7], H. Bourne[7]

[1]University of Illinois at Urbana-Champaign, Electrical and Computer Engineering Department, 306 N. Wright St., Urbana, IL, USA, 61801
[2]Embry-Riddle Aeronautical University, 1 Aerospace Boulevard, Daytona Beach, FL 32114-3900, USA
[3]Andes Lidar Observatory, Cerro Pachon, Chile
[4]La Serena University, Benavente 980, La Serena, Coquimbo, Chile
[5]NOIR Lab, Gemini South Observatory, La Serena,Chile
[6]Utah State University, Logan, UT 84322, USA
[7]Colorado State University, Ann and H. J. Smead Aerospace Engineering Science Department, 3775 Discovery Dr., Boulder, CO 80304, USA

Key Points:

- Several eclipse–induced events are observed by mesosphere and lower thermosphere sounders.
- eclipse–induced events are not directly generated in the MLT.
- A spectacular fast, bow–shaped gravity wave is observed in nightglow images, MTM brightness, lidar temperature and sodium density.

Corresponding author: Fabio Vargas, fvargas@illinois.edu

Abstract

This paper presents the results of a campaign covering a week of observations around the July 2, 2019, total Chilean eclipse. The eclipse occurred between 1922–2146 UTC, with complete sun disc obscuration happening at 2038–2040 UTC (1638–1640 LT) over the Andes Lidar Observatory (ALO) at (30.3°S,70.7°W). Observations were carried out using ALO instrumentation to observe eclipse–induced effects on the mesosphere and lower thermosphere region (MLT) (75–105 km altitude). Several mesosphere-sounding sensors were utilized to collect data before, during, and after the eclipse, including a narrow-band resonance-fluorescence 3D winds/temperature Na lidar with daytime observing capability, a meteor radar observing horizontal winds continuously, a multi-color nightglow all-sky camera monitoring the OH(6,2), O_2(0,1), O(^1S), and O(^1D) emissions, and a mesosphere temperature mapper (MTM) observing the OH(6–2) brightness and rotational temperature. To complement our dataset, we have also utilized TIMED/SABER temperatures and ionosonde electron density measurements taken at the University of La Serena's Juan Soldado Observatory. We discuss the effects of the eclipse in the MLT, which can shed light on a sparse set of measurements during this type of event. Our results point out several effects of eclipse–induced changes in the atmosphere below and above but not directly within the MLT. These effects include an unusual fast, bow–shaped gravity wave structure in airglow images, MTM brightness as well as in lidar temperature, strong zonal wind shears above 100 km, the occurrence of a sporadic E layer around 100 km, and finally variations in lidar temperature and density and the presence of a descending sporadic sodium layer near 98 km.

1 Introduction

Since Chimonas and Hines (1970a, 1970b) original prediction followed by mathematical derivation of Chimonas (1974), extensive campaigns were undertaken to look for evidence of waves induced by solar eclipses all way from the troposphere to the ionosphere. This has been a difficult task, as pointed out by Eckermann et al. (2007), declaring that direct observational evidence for eclipse-generated waves and bow waves is yet to be seen.

The effects of solar eclipses on the middle and upper atmospheric layers and in the ionosphere are well documented in the literature. It has been theorized that during a solar eclipse, the fast motion of the Moon's shadow across the Earth should cause a wave in the upper atmosphere in a similar fashion to a bow wave developing in front of a boat (Chimonas & Hines, 1970a). However, in the atmosphere, the cold region inside the shadow acts as a sinkhole that pulls the air ahead (Harding et al., 2018).

Chimonas (1974) modeled that the supersonic motion of the Moon's shadow across the Earth would generate a bow wave, a disturbance in the neutral atmosphere which would grow to an observable magnitude at ionospheric heights. Although the original focus was on the reduction in ozone heating in the stratosphere, models have subsequently shown that a significant large-scale wave is also expected to be seen in the thermosphere (e.g., Harding et al., 2018). Even if the generation of a large-scale wave in the upper atmosphere caused by a solar eclipse was predicted, experimental evidence remains sparse and comprises mostly indirect observations.

Although the vast majority of eclipse studies focus on ionospheric effects (e.g., Rishbeth, 1968; Rishbeth & Garriot, 1969; Le et al., 2009), the neutral atmospheric effects are also believed to be significant (e.g., Ridley et al., 1984; Eckermann et al., 2007). For instance, the impact of solar eclipses on weather and meteorological conditions has been studied by Mohanakumar and Sankaranarayanan (1982). Also, the reduction in radiative heating at all altitudes changes the temperature, wind, and composition of the neutral atmosphere, with the most significant neutral response expected to occur in the thermosphere. The thermospheric response should cause additional

secondary ionospheric effects, in addition to the direct photochemical responses, through ion-neutral coupling and chemistry (e.g., Roble et al., 1986; Müller-Wodarg et al., 1998).

This study presents observations gathered during a major solar eclipse passing over Chile on July 02, 2019, above the Andes Lidar Observatory location. The results show remarkable events associated with this total solar eclipse, such as the detection of a fast bow–shaped wave observed in the OH nightglow images from 2328 UTC to 0014 UTC after the end of the eclipse, the appearance of a descending sporadic Na layer detected in lidar temperature and density, the evident bow wave-induced perturbation on the detected sporadic Na layer, eclipse–induced zonal wind shears, and finally eclipse–induced sporadic E layer at about 100 km altitude. We present the results of each of these effects and discuss their possible causes and sources in the vicinity of the mesosphere and lower thermosphere (MLT) region.

2 Instrumentation

The Andes Lidar Observatory (ALO), Chile, is a facility supported by the National Science Foundation of the United States since 2009. The facility is located over the Cerro Pachon Mountain, 60 miles away from La Serena, and sits at 2,300 meters above sea level. Optical observation conditions are optimum for more than two-thirds of the year as cloudiness and humidity are low, and city lights contamination is minimized by the surrounding mountains.

Plans for a campaign to observe the total Chilean Eclipse initiated one year early to allow time to install a new meteor radar system and deploy a Faraday filter permitting daytime lidar measurements of sodium density and mesospheric temperatures (e.g., Harrell et al., 2010). Fig. 1 depicts the totality path crossing the area over ALO.

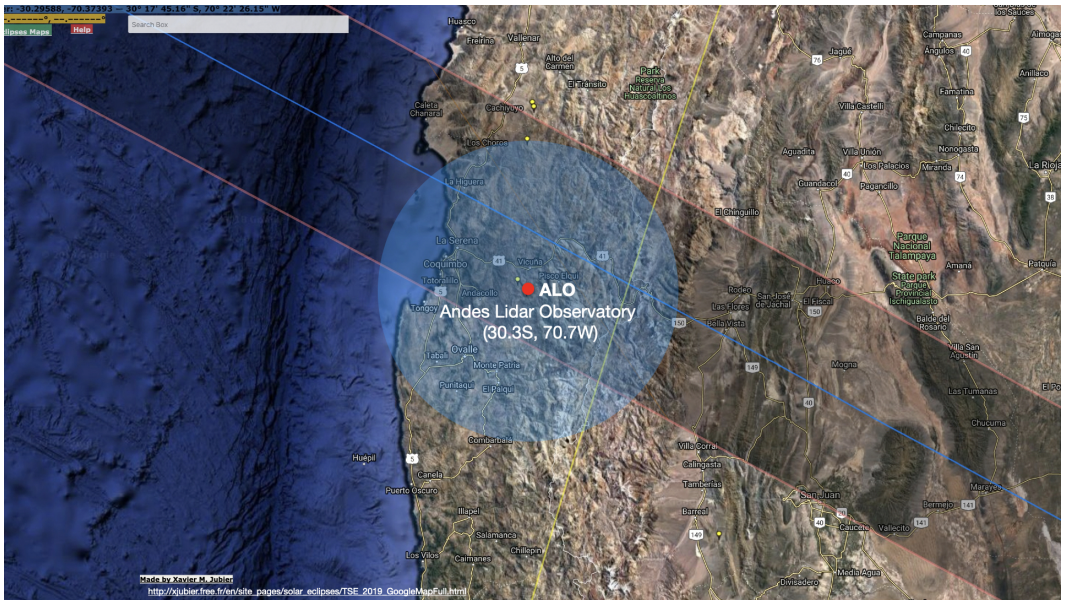

Figure 1. Eclipse path over the Andes Lidar Observatory. The red dot shows the location of the observatory and the blue circle the field of view of the new meteor radar system.

Day and night observations were carried out during seven days around eclipse day. Lidar and meteor radar ran day and night continuously, while optical cameras operate from sunset to sunrise. In this paper, we focus on eclipse-associated events

in the MLT only, although measurements of the ionosphere were also taken and are available elsewhere (e.g., Bravo et al., 2020).

2.1 Airglow All-sky Imager

The ALO all-sky imager (ASI) is equipped with an Apogee Alta 6 CCD camera and a 30 mm fish-eye lens. It records several nightsky emissions over an 180° field of view allowed by fisheye and telecentric lens system. Apogee camera houses a Kodak KAF-1001 CCD sensor with a 1024 x 1024 array and 24 µm pixel pitch with a $24.6 \times 24.6\,mm^2$ active imaging area. High sensitivity is achieved by combining >72% QE @560nm, low noise readout electronics, and deep TE cooling down to -20°C. The ASI interference filters permit to record images of the OH(6–2), O_2(0,1), O(^1S), and O(^1D) nightglows emissions during moonless periods. Images are integrated on a continuous cycle every ∼45 seconds (75 seconds of the ionosphere redline emission), with each particular filter position visited every 3.5 min. More ASI features and specifications are given in Vargas et al. (2020).

2.2 Mesosphere Temperature Mapper

The Utah State University mesosphere temperature mapper (MTM) measures the brightness and rotational temperature of the mesospheric hydroxyl molecule nightglow emission over a 90° field of view centered on the zenith. MTM measurements are used to determine the temperature perturbations induced by atmospheric gravity wave activity. Although the MTM image frame has 1024×1024 pixels produced by a back-illuminated CCD detector, an (8×8) binning operation reduces the MTM image size to 128×128 pixels to improve the signal-to-noise ratio. The CCD detector is mounted below a telecentric lens system and a set of narrow-band interference filters to measure the $P_1(2)$ and $P_1(4)$ lines of the OH(6,2) band at 840 and 846.5 nm, respectively, and the sky background intensity at 857 nm. Each emission is observed for 30 sec followed by a background measurement, resulting in a 2 min cadence and a zenith pixel footprint of 0.9x0.9 km at 90 km altitude. Rotational temperatures are computed using the ratio method in Meriwether (1984), show precision of 0.5% and 1–2 K in brightness and rotational temperature measurements, respectively. Complete details of the MTM design and calibration can be found in Pendleton Jr. et al. (2000) and Taylor et al. (2001).

2.3 Na wind/temperature Lidar

The ALO lidar system is a narrow-band resonance-fluorescence Na lidar. The lidar transmits a nominal power of 1.5 W via a source of coherent light locked at the Na resonance frequency at the D2a line, using the three-frequency technique (Krueger et al., 2015), where the central frequency (fo) is shifted by ±630 MHz to obtain the shifted frequencies f+ and f- in a sequence to produce the optical excitation of the mesospheric sodium layer around the Na D2a linewidth, enabling the production of an artificial beacon source. In May 2014, the system was upgraded by replacing the old Coherent Ring Dye Laser with a high-power amplified diode laser (TA-SHG from Toptica Photonics) as the master oscillator (A. Liu et al., 2016), and the receiver system was improved with a more efficient optical design (Smith & Chu, 2015). The upgraded system runs now in nearly uninterrupted nightly lidar operations with signals of over 1000 counts per laser pulse from the Na layer at about 0.4–0.6 Wm^2 power aperture product. These improvements result in a much more reliable and stable system with several times higher signals, making it possible to achieve many more nights of measurements with better data quality and higher resolutions.

The lidar performs nightly measurements of temperature, line-of-sight (LOS) winds, and Na density profiles between 80 and 105 km, depending on the ratios among the

back-scattered signals at the three monitored frequencies. The ALO lidar system is equipped with four 75-cm diameter telescopes pointing toward zenith and 20° off-zenith to south and east directions. To derive the LOS winds and temperature, raw lidar photon counts are typically processed at 60 sec (90 sec on some nights) integration time and 500-m range resolution, but the integration time for lidar scans varies between campaigns which depend on the signal-to-noise ratio retrieved from the photon returns. The root mean square (RMS) errors for temperature and LOS winds due to photon noise are respectively 1.4 K and 1.1 m/s at the Na layer's peak. These errors increase quickly beyond this altitude range and are 2.2 K and 2.0 m/s at 85 and 100 km.

2.4 Meteor Radar

The new ALO meteor radar was deployed in June 2019, just in time before the eclipse. The radar is an Enhanced Meteor Detection Radar built and installed by ATRAD Pty Ltd, Australia. The radar has a nominal peak power of 40 kW, higher that many meteor radars currently in operation. Combined with the quiet radio environment around ALO, this radar is able to routinely detect over 35,000 meteor echoes per day, compared to a few thousands up to 20,000 for other systems (Fritts et al., 2012; L. Liu et al., 2017). The location of the transmitter and receiving antennas are next to the ALO building, thus the radar measures neutral winds in the same volume as the lidar, but with a 24/7 coverage.

2.5 Juan Soldado Observatory Ionosonde

The ionosonde system is located the La Serena University's Juan Soldado scientific facility (29.9°S, 71.3°W), Chile. The system, deployed approximately 10 km north of La Serena, is an IPS-42 ionosonde operated by Inter-University Center for Upper Atmosphere Physics (CInFAA), and is located about 60 miles from the ALO facility. A full description of the ionosonde can be found in Bravo et al. (2020). Also, a comprehensive characterization of the eclipse's effects in the ionosphere near ALO and other two observatories are thoroughly discussed in Bravo et al. (2020).

2.6 TIMED/SABER

TIMED (Thermosphere Ionosphere Mesosphere Energetics and Dynamic) mission was launched in December 2001, and is still operating some of the instruments over 19 years later. SABER measurements of OH Meinel band emissions are a routine data product, including rotational temperature distributions (Marsh et al., 2006). We have retrieved measurements of the SABER (Sounding of the Atmosphere using Broadband Emission Radiometry onboard of TIMED Explorer mission (Russell et al., 1999; Mlynczak, 1997; Yee et al., 1999) to further investigate eclipse–induced c the MLT.

3 Mesosphere Measurements and Results

3.1 Allsky imager measurements

3.1.1 Bow Wave, scenario 1

During the eclipse campaign, nightglow images were taken every night over the campaign. On the evening of July 02, observations began at 2300 UTC after the eclipse ended. Fig. 2 shows the occurrence of a spectacular and rare wave event displaying bow–shaped wavefronts traveling eastward at an apparent horizontal phase speed of 104–243 m/s. Luckily, the wave entered the imager field of view (FOV) right after the observations began. Fig. 2 shows a sequence of time-difference images of the OH emission where the contrast of the wave in the airglow brightness was the largest. The image sequence goes from left to right and top to bottom in time. The frames are dis-

torted due to the camera fisheye lens but permit better visual inspection of wave's eastward horizontal propagation. However, further wave feature analysis was carried out using dewarped image frames. Bow–shaped wavefronts are more discernible near the south-east edge in the image taken at 0007 UTC, a few minutes after the wave crossed the image's zenith.

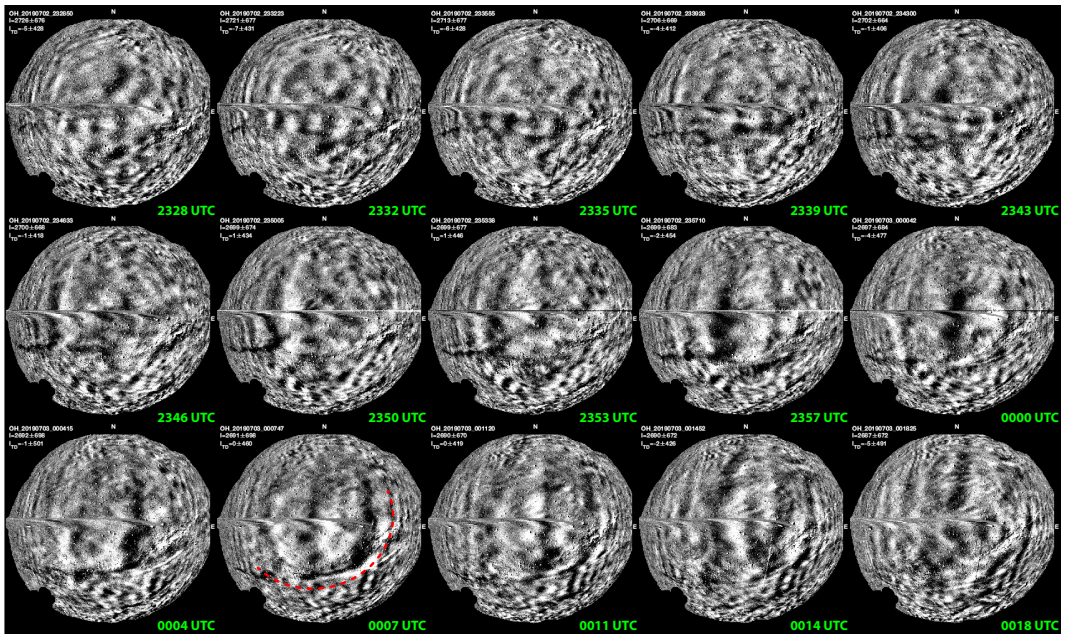

Figure 2. Sequence of time-difference OH airglow images showing the wavefronts of a fast, bow–shaped gravity wave on Jul. –, 2019 traveling eastward. The time spans from 2328 UTC to 0018 UTC. The red-dashed line on the image of 0007 UTC shows the bow-shaped wavefront.

Calculation of features from dewarped frames reveals a wave with a horizontal wavelength of 150.0 km. By taking the vertical and horizontal lines of the sequence of dewarped image frames from 2328 UTC to 0018 UTC, we have built east-west (zonal) and north-south (meridional) keograms, allowing further analysis of the wave features. The resulting keograms are presented in Fig. 3, where the green-dotted lines delimit the bow wave structure. The zonal keogram show tilted wavefronts since the wave is traveling eastward, while the meridional keogram show roughly the instant the wavefronts crossed the image zenith. From the tilt of the green-dotted lines in Fig. 7a, we infer that the wave structure traveled 512 km in ∼35 minutes, allowing to estimate an apparent horizontal phase speed of 243.0 m/s and apparent period of 10.3 minutes. The considerable phase speed of the wave (close to the sound speed of 270 m/s) is rarely seen over ALO, suggesting that the bow wave could have been excited by eclipse–induced cooling effects on the neutral or ionized atmosphere below or above the wave occurrence altitude.

Considering an eastward wave propagation on top of a zonal wind of 20 m/s (Fig. 6), we estimate a bow wave intrinsic period of 11.2 minutes. Using the dispersion relation and the linear gravity wave theory, we can calculate a bow wave vertical wavelength of 67 km and a vertical group velocity of 97.7 m/s (5.8 km/minute). For reference in the discussion section, we label the wave feature obtained utilizing the keograms as scenario 1 parameters.

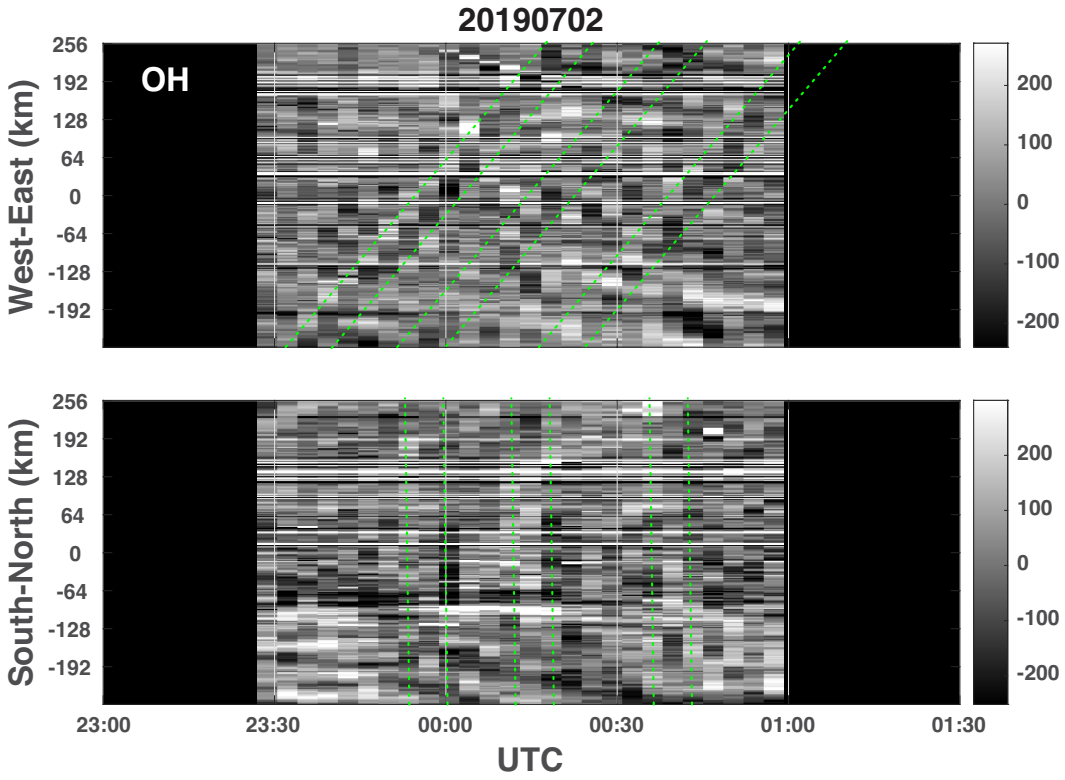

Figure 3. (a) zonal and (b) meridional keograms built with OH airglow images taken on July 2–3, 2019. Green-dotted lines depict the wave fronts of the fast wave crossing the imager field of view with apparent phase speed of 240 m/s.

3.2 Mesosphere temperature mapper measurements

3.2.1 Bow Wave, scenario 2

Fig. 4a presents the MTM measurements during three nights around the eclipse day. The OH(6,2) brightness is represented by the continuous black lines and the rotational temperature by blue lines. The vertical red lines in Fig. 4a represent the beginning, total obscuration, and ending of the eclipse event over ALO. Measurements taken on the evening of July 02, 2019, are presented in Fig. 4b. In the nights prior and after the eclipse, the rotational temperature decreases fast from >200 K at the beginning of observations to <180 K by 0200 UTC. Similarly, the OH brightness decreases from 11×10^4 counts to $<6\times10^4$ counts by 0200 UTC. However, on the evening of July 02, the temperature remains high ($\sim$200 K) until 0400 UTC and then decreases to <180 K rapidly, while the OH brightness remains high until 0200UTC and then decreases slowly, reaching $<6\times10^4$ counts at 0400 UTC.

In Fig. 4b, the red-dotted box indicates the occurrence of a large-amplitude oscillation (15.4% peak-to-peak) in nightglow brightness. However, the rotational temperature oscillation shows an amplitude of 2.5 K (1.2% peak-to-peak). The OH brightness is more responsive of wave perturbations compared to that in rotational temperature because the OH photochemistry depends on various perturbed mesospheric constituents such as the atomic oxygen, molecular oxygen, and molecular nitrogen as well as the perturbed temperature (G. R. Swenson & Gardner, 1998; Vargas et al., 2007). This

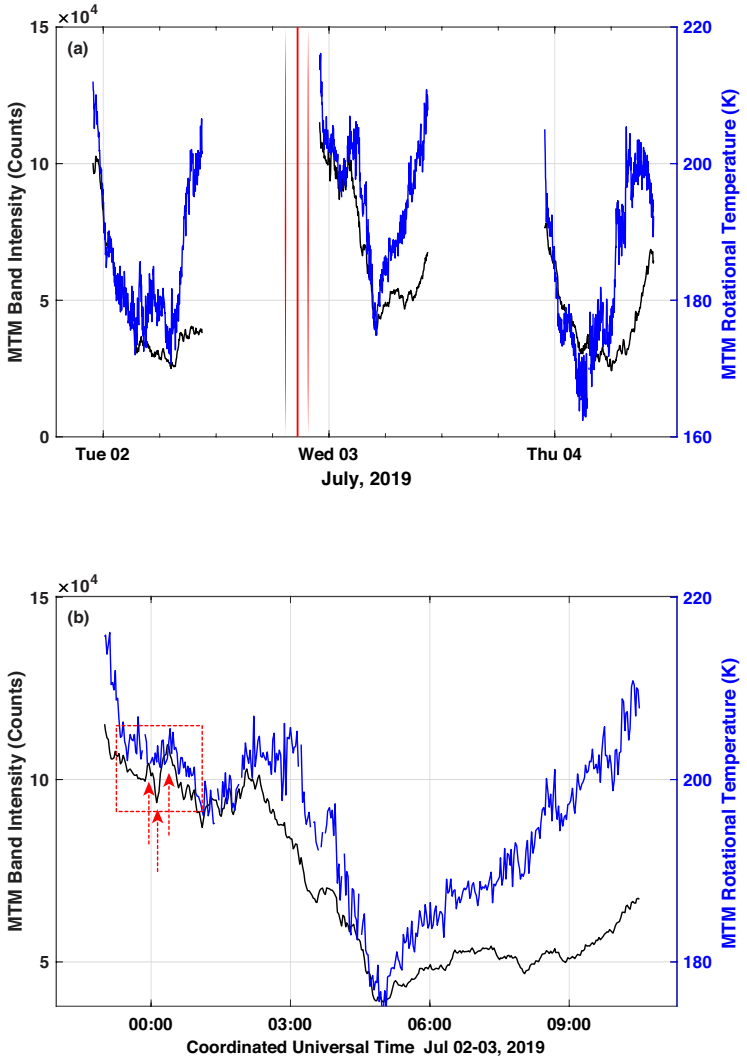

Figure 4. Mesosphere Temperature Mapper. MTM rotational Temperature is warmer than the night before and after the night following the eclipse. The red-dotted square indicates a strong oscillation in the OH intensity caused by the fast, bow wave shown in the airglow images. The vertical red lines in (a) indicate the beginning, total obscuration, and the end of the eclipse.

brightness response is large for waves of long vertical wavelength (>25 km) (Vargas, 2019), which is the case for the bow–shaped wave, as shown in the discussion.

The vertical, red-dashed arrows indicate the wave's ridges and troughs. Notice the first wavefront crossing zenith instants before 0000 UTC. Notice in Fig. 2 the bow wave's horizontal structure across the image zenith at 0000 UTC. The wave amplitude in OH brightness is large at 0014 UTC, which can be confirmed in Fig. 2 as well. From the time difference between the salient brightness peak, we have estimated an apparent wave period of 24 minutes. Taking into account the 150 km horizontal wavelength calculated from the OH images, we obtain a bow wave apparent phase speed of 104 m/s.

Again, as the bow wave travels eastward over a zonal wind of ∼20 m/s, the intrinsic phase speed is estimated in 84 m/s, and the intrinsic period in 29 minutes. The

bow wave is fast compared with regularly observed waves over ALO that usually show horizontal phase speeds of <60m/s (but usually with shorter wavelengths). However, the bow wave is still in the gravity wave branch since the estimated sound speed in the MLT for the eclipse night was 276 m/s. Using the gravity wave dispersion and the gravity wave linear theory, we can calculate the bow wave's vertical wavelength in 25 km and a vertical group velocity of 13.8 m/s (0.8 km/minute). We label the wave features obtained here as scenario 2 parameters. Table 1 summarizes the bow wave features obtained in scenarios 1 and 2.

Table 1. Estimated features of the bow wave observed in the airglow.

	λ_h (km)	λ_z (km)	τ_o (min)	τ_i (min)	c_o (m/s)	c_i (m/s)	c_{gz} (km/min)	c_{gz} (m/s)
scenario 1	150	67	10.3	11.2	243	223	5.86	97.7
scenario 2	150	25	24	29	104	84	0.8	13.8

3.3 Lidar measurements

Fig. 5a and 5b show lidar sodium densities and temperatures for the three days centered at the eclipse event, respectively. Daytime measurements were made possible by a narrow-band, magnetic effect, Faraday filter receiver (Harrell et al., 2010) used from sunrise to sunset. The regular optical interference filter receiver was used for nighttime from sunset to sunrise. No changes were necessary on the lidar transmitter, and switching from daytime to nighttime lidar observation mode was carried out manually. The vertical red lines in Fig. 5 indicate the eclipse start, total obscuration, and end. The eclipse totality occurred at 1638 LT (2038 UTC) over ALO.

Fig. 5c and 5d show lidar measurements for the eclipse day only. At first sight, the measurements indicate consistency between day and night, meaning that what is occurring during the day continued during the night, even though day measurements are noisier as a consequence of the Faraday filter that rejects daylight radiation and with that some portion of the Na backscatter from the transmitted lidar beam pulses. During the eclipse totality, both sodium density and ambient temperature do not present significant enhancement, although the sodium density is slightly larger, around 86–88 km. The sodium layer is relatively narrow ($\sim$4 km) up to the eclipse start, widening vertically to 10 km by totality. The diurnal tide is present and is more evident in temperature, where its descending phase is more noticeable. The red-dotted arrow labeled "Diurnal Tide" helps to localize the wave descending phase in Fig. 5c–d.

The mesopause region maintained its diurnal evolution. After sunset, we observed the region's cooling above 90 km and a sporadic Na Layer (Na_s). A faint signature of the Na_s is noticeable earlier around the eclipse totality at 98 km altitude. The Na_s descends from 98 km at 2040 UTC to 94 km at 2330 UTC when its density is more prominent, and we notice that the descending phase speed of the Na_s resembles that of the diurnal tide in Fig. 5c. After 2330 UTC, the Na_s dissipates, although Na's more prominent density peak is visible later at 0030 UTC at 96 km. Around 2330 UTC, when the Na_s is stronger at 94 km, we also notice a strong oscillation of 20–25 minutes period in both Na_s density and ambient temperature.

In Fig. 5d, the temperature clearly shows a descending phase structure appearing near 100 km at 2140 UTC, 94 km at 2330 UTC, and 88–90 km at 0000 UTC. We assume this descending structure is associated with the bow wave seen in the airglow images. The red-dotted arrow labeled "bow wave" helps to visualize the wave descend-

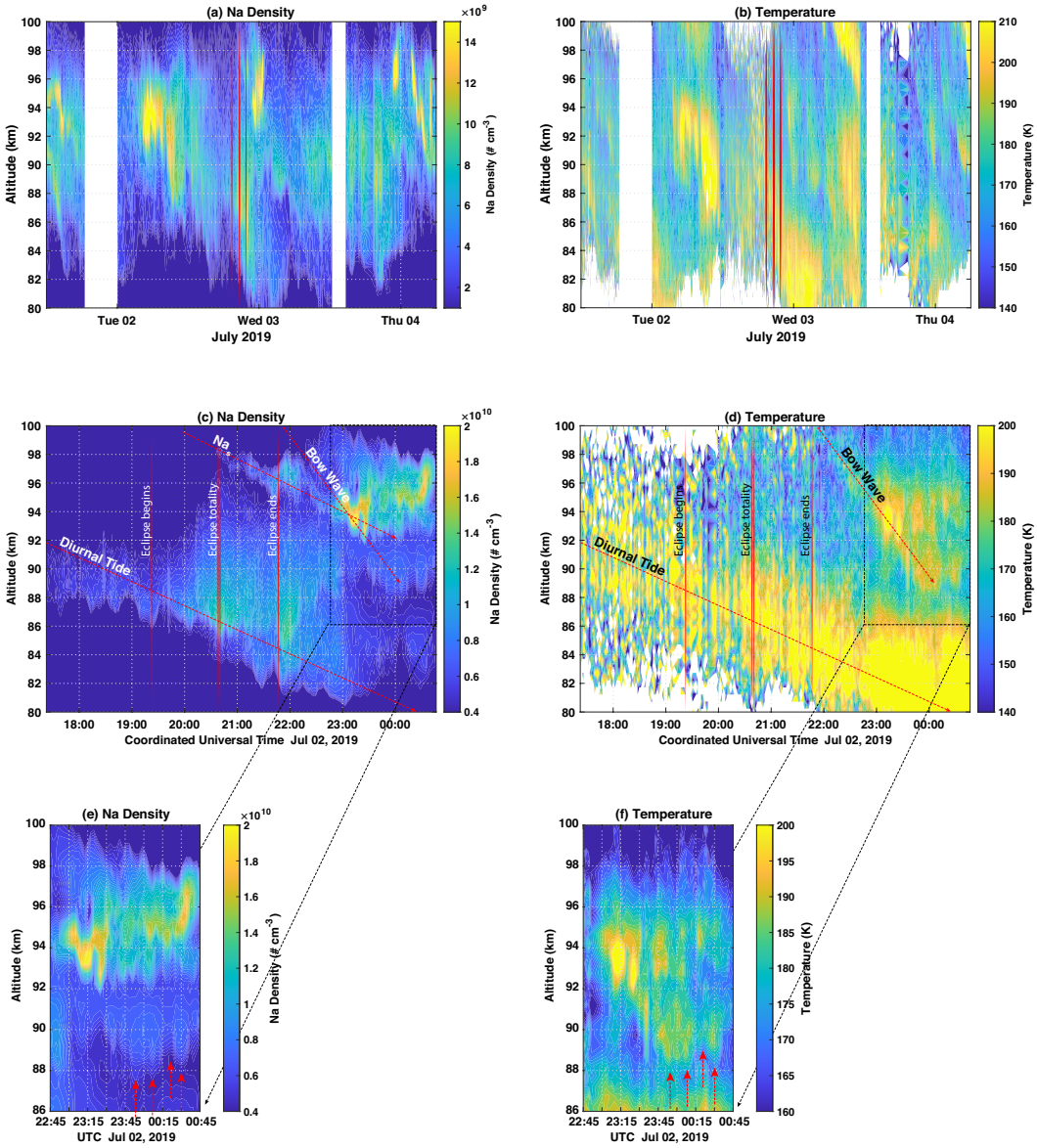

Figure 5. Lidar measurements. The insets (e) and (f) show oscillatory features in the Na density and temperature associated with the bow–shaped wave also seen ∼30 minutes later in the airglow images and MTM brightness signal. The vertical red lines indicate the beginning, total obscuration, and the end of the eclipse.

ing phase structure. The insets in Fig. 5e-f are close-ups of the interest region highlighted by the black-dotted boxes in Fig. 5c–d. The red-dotted arrows at the bottom of Fig. 5e–f indicate ridges and troughs of the oscillation at around 87 km with a period of 20–25 minutes as well.

3.4 Meteor radar measurements

Fig. 6 shows the meteor radar measurements taken around the eclipse event. We notice the zonal wind variance is more significant in the 70–85 km range, while the meridional wind shows a more considerable variance in the 85–100 km range. Tidal

oscillations are also present in both wind directions. During the eclipse day (Fig. 6c–d), we notice an apparent disruption of the tidal oscillation patterns at 90–110 km altitude around the eclipse start time. As the eclipse ends, the zonal wind decreases in magnitude to about 20 m/s at 87 km altitude and continues in that range until 0200 UTC on the next day. Observe the 80–100 m/s jet occurring near 75 km level on the zonal wind, which is not apparent on the meridional wind. The meridional wind is weak and directed southwards on average, although it is northward during the eclipse times in the 95–110 km range and at the 75 km level from 2200 UTC onward.

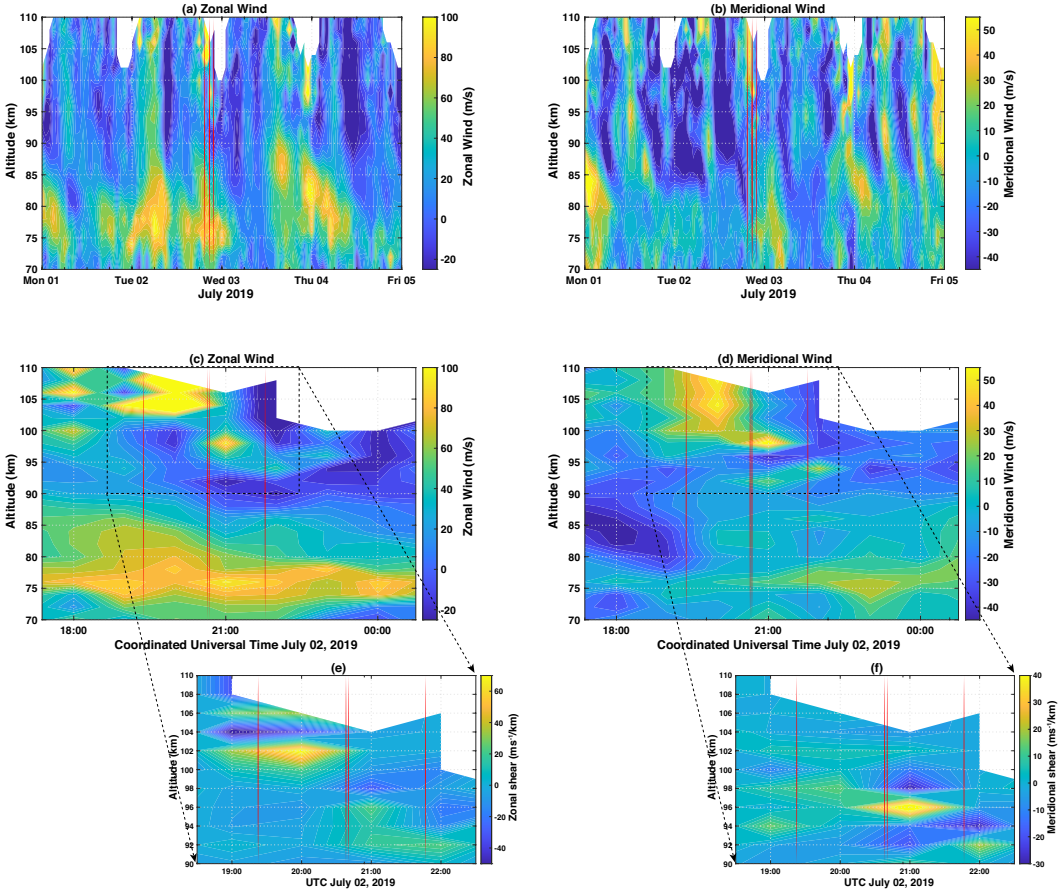

Figure 6. Zonal and Meridional time vs. altitude cross-section of horizontal winds from measurements of the new ALO meteor radar system. The insets (e) and (f) are the zonal and meridional wind shear cross-sections for the region of interest highlighted by the black-dotted boxes. The vertical red lines indicate the beginning, total obscuration, and the end of the eclipse.

The black-dotted squares highlight the region of interest, showing the zonal wind with a magnitude of about 180 m/s at around 105 km and -20 m/s at 90 km. The meridional wind also shows substantial variation over the 90–110 km range, with significant changes occurring about 30 minutes earlier than the eclipse totality within 100–110 km altitude range. Because of the substantial variation of the wind magnitude in height during the eclipse, we have also calculated the zonal and meridional wind shears presented in the insets (Fig. 6e–f). The zonal wind shear is strong (>60 ms^{-1}/km) at 102 km by 2000 UTC about 30 minutes earlier the eclipse totality, and also at 104 km with a magnitude >40 ms^{-1}/km. The meridional wind shear is much weaker and presents magnitudes of 30–40 ms^{-1}/km around 96 km about 20 minutes after the totality.

4 Discussion

We have shown indications of the influence of the eclipse in the MLT, namely, the detection of a fast, bow–shaped wave traveling eastward in OH nightglow images as well as the appearance of a descending sporadic Na layer in our lidar scans, and also a strong wind shear in the zonal wind 30 minutes prior the eclipse totality. We investigate the possibility that these features were triggered by eclipse–induced changes on the lower stratosphere (from the cooling of the ozone layer) and on the ionosphere (from electron temperature cooling and recombination rate changes).

4.1 Direct effects of the Eclipse in the MLT

To evaluate the eclipse effects on the MLT, we have first retrieved SABER temperate measurements (Fig. 7) along the 230°E meridian for the days before, during, and after the eclipse around 1853 UTC. During the eclipse day, SABER measurements were retrieved as close as possible to the eclipse totality, about 12° from the total obscuration region at (19°S, 242°E). SABER sampled an area within a 50–90% obscuration to the west of the totality point. SABER temperatures during the eclipse day (Fig. 7b) indicate a colder (∼97 km) and warmer (∼105 km) region at ∼20° latitude depicted by the black-dashed box. Fig. 7d shows an inset of the same interest region indicating that the area was 35% colder and 30% warmer than the average of the control days (before and after the eclipse) at the given reference altitudes. Over ALO, the eclipse totality occurred at 2038–2040 UTC, but SABER measurements were only taken in the morning of Jul 03 at around 0455 UTC.

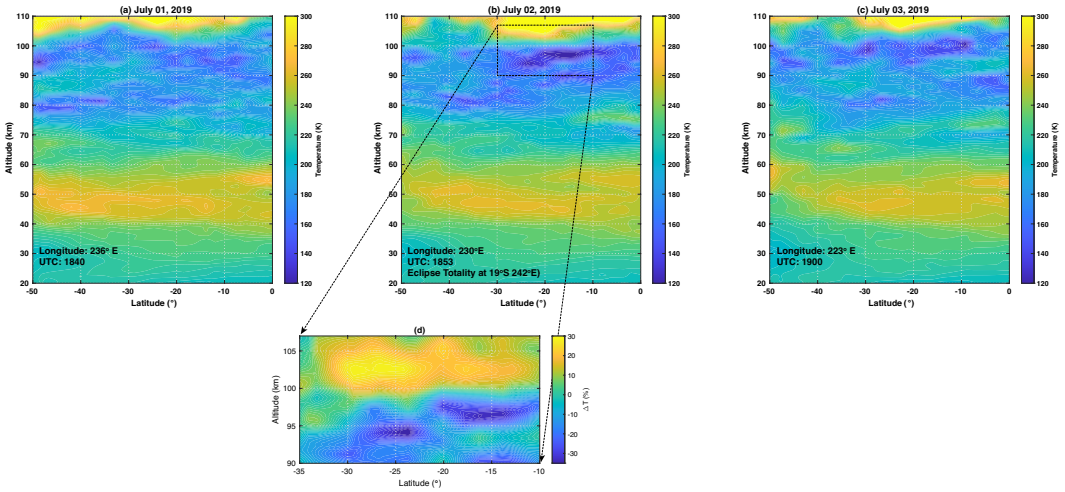

Figure 7. SABER Near Eclipse totality

Although it seems reasonable to consider the temperature changes in Fig. 7d a direct consequence of the eclipse, a closer examination of lidar temperatures measured during the eclipse totality over ALO allows a different interpretation. The daytime Lidar scans recorded over ALO around the eclipse totality in Fig. 5d indicates neither cooling nor warming induced by the eclipse in the MLT temperature, suggesting that the cold/warm regions would not be a direct consequence of eclipse. Moreover, similar cold/warm structures in the MLT are also present in Fig. 7c but not in Fig. 7a around the same region of interest. Thus, the observed cooling/warming in the MLT can not be directly associated with the eclipse conclusively. However, indirect effects of the eclipse in the MLT are possible.

It could be possible, for example, that the observed cooling/warming temperatures be caused by waves coming from above or below the MLT since the highlighted area in Fig. 7b resembles a vertical oscillating structure. Previous publications show the occurrence of gravity waves in the ionospheric E region induced by eclipse cooling. For instance, some of the ionospheric wavelike disturbances result from gravity waves excited in the thermosphere. Jakowski et al. (2008) reported the ionospheric effects of the 3 October 2005 solar eclipse over Spain. They found that the ionosphere responded by (a) an approximately 30 total electron content (TEC) units decrease (as measured by GNSS TEC) resulting from an NmF2 decrease, an hmF2 increase, and an initial slab thickness increase, and (b) a small-amplitude gravity waves with an approximately 6-minute period. The former was probably associated with a competing slab thickness increase and regional cooling, while the latter had no apparent source, that is, either in the thermosphere ($\sim$180 km altitude) or somewhere in the middle atmosphere.

Similarly, Chen et al. (2011) focused on the study of sporadic E_s layer effects over Wuhan, China (30.4°N, 114.3°E), using simultaneous observations from an ionosonde and an oblique backscattering sounding system. They found the exceptional occurrence of the E_s layer during the eclipse with a periodicity of 35 min for both the electron concentration and the spread E_s drifting velocity. They suggested that a gravity wave deformed the E_s layer and produced wave-like structures responsible for off-vertical E_s echoes. Thus, we hypothesize that the strong temperature oscillation in the MLT observed by SABER is possibly due to a downward oscillation excited in the ionosphere due to eclipse–induced cooling.

4.2 Bow wave source and vertical propagation conditions

We can not rule out the possibility of indirect eclipse effects on the MLT due to waves coming from below. The fast bow wave observed clearly in the OH images in Fig. 2 has properties that support its excitation below the MLT. It has been suggested that the cooling action resulting from a solar eclipse can generate bow waves as the shadow of the moon passes across the surface of the earth at a supersonic speed (Chimonas & Hines, 1970b; Chimonas, 1974; Beer & May, 1972). This mechanism seems capable of generating the observed continuous atmospheric wave spectrum in the upper atmosphere. The rationale is that, for instance, if the supersonic shadow of a solar eclipse would have a similar effect as that of the terminator (e.g., Beer, 1973; Raitt & Clark, 1973; Beer, 1978). The terminator is supersonic between +45° latitude at all altitudes below the mesopause, but the supersonic area increases to about $\pm 55^\circ$, but above 100 km it is no longer supersonic because the high temperatures in the thermosphere increase the sound speed to a value greater than the earth's rotational speed. Thus, it seems likely that the ozone heating region and the bottom of the molecular oxygen heating region will generate atmospheric waves every twelve hours due to the terminator and also when there is a solar eclipse. Bow waves should be induced by extreme impulses such as those caused by eclipses initiating rapid atmospheric cooling. An impulsive event has been reported by Harding et al. (2018) in thermospheric wind measurements of the September 2017 Great American Eclipse. It has also been simulated by Huba and Drob (2017), showing the effects of that eclipse on thermospheric quantities such as electron density and temperature, O+ velocity, and total electron content near the eclipse totality location and at its conjugate point.

We have determined the bow wave properties from the wave signature analysis on the OH airglow images, MTM, meteor radar winds, and finally lidar temperatures and sodium density. Assuming that the bow wave was generated by impulsive cooling in the ozone layer near the peak of stratosphere, 40 km below the MLT, and considering homogeneous both the wind and temperature, it would take, under scenario 1 (Table 1), about 6.9 minutes for the bow wave to travel from the excitation re-

gion up to the detection region in the peak of the OH layer at 87 km around 0000 UTC. Under scenario 2, the bow wave would take 48 minutes to cover the same 40 km vertical distance. Alternatively, the bow wave could have also been excited around 20 km in the tropopause water vapor layer due to eclipse–induced cooling, that is, 67 km below the OH layer peak. Under scenario 1, it would take about 11.5 minutes for the wave to cover the 67 km distance, whereas it would take 80.0 minutes for the wave to cover the same distance under scenario 2 conditions.

The bow wave excitation indeed occurred to the west of ALO since it appears first in the west corner to the OH airglow images and travels eastward. Assuming the horizontal wind is homogeneous for a moment, we can calculate the distance traveled horizontally by the wave from its excitation sources below the OH layer. Under the assumption of wind homogeneity, the horizontal phase velocity equals the horizontal group velocity. This way, in scenario 1, the wave would have been generated 92 km the west of ALO for the stratosphere generation case and 154 km away for the water vapor layer generation case.

For scenario 2, the wave would have been generated 242 km away from ALO for the stratospheric case and 403 km away for the water vapor layer generation case. Considering an eastward wave propagation on top of a zonal wind of 20 m/s (Fig. 6), we estimate a bow wave intrinsic velocity to be 223 m/s. The hydrostatic assumption of the dispersion relationship (G. Swenson et al., 2003) defines the vertical wavelength as $\lambda_z = \frac{c_i}{N} = 67$ km, where N is the Brunt-Väisälä frequency. These parameters are consistent with the intrinsic attributes of the semidiurnal tide. The large eastward motion of the apparent two brightness bumps in the OH airglow could be an artifact associated with coupling with the semidiurnal tide. The data is marginal and inconclusive regarding the cause.

Our calculations show that it is not possible to conciliate the wave detection time in the OH airglow (from 2330 UTC to 0018 UTC) with the times and locations of wave excitation in the lower atmosphere, at least using the simplistic approach where the horizontal wind and temperature are homogeneous. Thus, we must realize that wind and temperature vary with altitude in such a way to make possible the detection of the bow wave by our sensors. Assuming a structured atmosphere, the linear wave theory shows that the bow wave vertical group velocity could have slowed down near leaky absorption regions, where the wave is partially absorbed but still can penetrate through after some time. This must have been the case for the bow wave propagation conditions in its path from the excitation altitude to the detection region.

Evidence of this is that the bow wave is propagating into the zonal wind in the MLT, which is not strong enough to absorb this relatively fast wave entirely. Notice the zonal jet in Fig. 6 near 75 km presenting a magnitude of <100 m/s, while the bow wave eastward apparent speed is 104 m/s, characterizing a leak absorption region just below the mesopause. Because of this, we can hypothesize the bow wave may have been generated in the lower atmosphere by an impulsive, eclipse–induced cooling of the ozone or water vapor layers in a location a few hundred kilometers away to the west, earlier than 1920–2140 UTC, the eclipse time over ALO. Another strong evidence that the bow wave was generated in the region below the MLT is seen in Fig. 5d that shows the bow wave's descending phase, suggesting that the oscillation is upward propagating.

Results from other investigators support this claim. For example, Kumar et al. (2016) using GPS and FORMOSAT-3/COSMIC satellite data taken during eclipses at 100% to 78% obscuration observed TEC oscillations with periods of 40–120 minutes associated with gravity waves generated in the lower atmosphere. Similarly, Paulino et al. (2020) has demonstrated the presence of mid-scale gravity waves associated with

the August 2017 great American solar eclipse in airglow measurements with observed periods of 152 minutes triggered ∼1618 km away from the observatory location in Brazil.

Using the bow wave characteristics found for scenario 2, we have investigated the vertical propagation conditions for the bow wave in the altitude range of 80–100 km. For that, we have inserted in the Taylor-Goldstein equation (Salby et al., 1996, pg. 449)

$$m^2 = \frac{N^2}{(u - c_o)^2} + \frac{u_{zz}}{(u - c_o)} - k_h^2$$

the bow wave parameters for scenario 2 (Table 1), preprocessed lidar temperatures, and meteor radar winds to obtain the bow wave vertical wavenumber in altitude versus time (Fig. 8). In the Taylor-Goldstein equation, N is the Brünt-Väisälä frequency, u is the background wind in the wave propagation direction, u_{zz} is the wind second derivative, and c_o and k_h are the observed horizontal phase velocity and the horizontal wavenumber, respectively.

Fig. 8 shows several patches of forbidden vertical propagation regions for an oscillation similar to the bow wave. The deep blue areas indicate $m^2 \leq 0$. Interestingly, the red-dotted box highlights a permitted vertical propagation region bounded by forbidden regions to the top and bottom, revealing a wave propagation channel. Coincidentally, the highlighted propagation channel coincides with the OH layer peak altitude observed by SABER for that same night but later morning hours (not shown). Also, the channel extends from 2300 UTC to 0130 UTC, within the bow wave detection time window in the OH airglow images. The propagation channel depicted in Fig. 8 also explains the weak signature of the bow wave in the brightness of O_2 and O(^1S) images, because these emissions are located at 92 km and 96 km, respectively, well above the permitted vertical propagation channel.

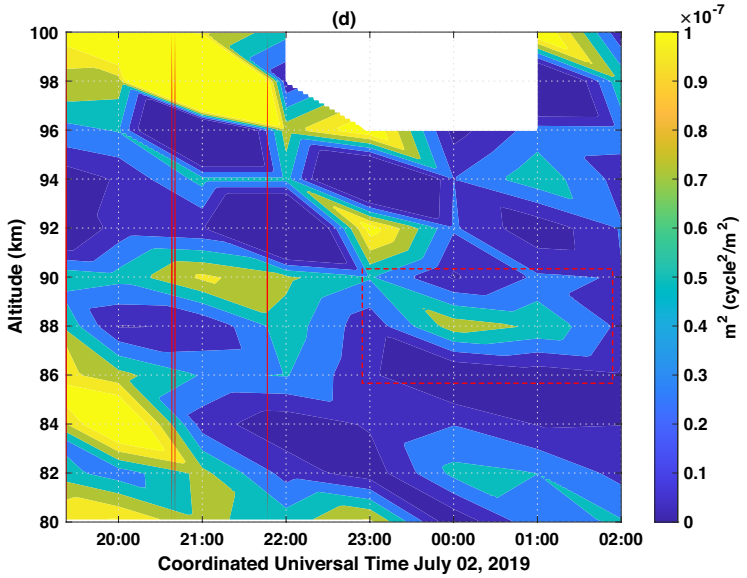

Figure 8. Bow wave vertical wavenumber variation with altitude due to structured wind and temperature across the MLT on Jul 02–03, 2019. The red-dotted box indicates a channel around the OH layer altitude between 85–90 km. The vertical red lines indicate the beginning, total obscuration, and the end of the eclipse.

Another possible source of the bow wave would be associated with the eclipse obscuration and subsequent cooling of the lower ionosphere regions. Goncharenko et al. (2018) shows that the electron and ion temperatures decrease by 100–220 K (electrons) and 50–140 K (ions), respectively, above 150 km, evidencing the ionosphere cooling during eclipse events. Chen et al. (2011) determine the presence of wave-like structures and traveling ionospheric disturbances (TIDs) during July 22, 2009, total solar eclipse over Wuhan, China. They assumed that the TEC perturbations (periods from 1.0–2.5 h) were entirely due to the obscuration of solar UV radiation, which led to varying ionization levels in the ionosphere. One of the early reports about the great American eclipse using a large set of observations was presented by Zhang et al. (2017). The experiment used observations from 2000 GNSS receivers to derive the TEC over North America. They have found an "unambiguous evidence" of ionospheric bow waves lasting approximately one hour with a wavelength of 300–400 km and a phase speed of 280 m/s originating from the totality region.

Furthermore, they noted supersonic ionospheric perturbations from the maximum solar obscuration, which were too fast to be associated with gravity waves or traveling ionosphere disturbances. Similar analyses by Sun et al. (2018) indicated that a "great ionospheric bow wavefront" (3000 km wide) was observed. The supersonic moon shadow-induced acoustic shock wave resulted in the bow wave trough and crest near the totality path. The acoustic shock wave and plasma recombination in the ionosphere controlled the bow wavefront formation rather than gravity waves excited by the moon shadow from the lower atmosphere. Furthermore, Eisenbeis et al. (2019), using 3000 GNSS receivers to determine the TEC, found that complete identification of eclipse-generated traveling ionospheric disturbances is possible using 3D fast Fourier transform analysis. They have shown that these disturbances exhibit wavelengths and periods of 50–100 km and 30 min, respectively, and 500–600 km and 65 min, identifying these oscillations as bow-type waves. Moreover, they suggested that these TIDs are what other researchers have identified as bow waves in Zhang et al. (2017) and Sun et al. (2018).

4.3 Connection between the observed E_s and Na_s Layers

The sporadic sodium layer showed in Fig. 5c points out the possibility of the bow wave generation above the MLT within the ionospheric E region. We have highlighted interest regions in Fig. 5c and Fig. 5d by the red-dotted arrows. The arrow labeled Na_s in Fig.5c indicates a descending feature that culminates in a strong sporadic layer at around 2300–2330 UTC. Note that about 2300–2330 UTC, the Na_s shows an oscillation with a period of 20–25 minutes, which is consistent with the bow wave periods determined using data from our airglow instruments. The Na_s oscillation associated with the bow wave also occurs in the MTM brightness (Fig. 4d). The bow wave descending phase is depicted by the red-dotted arrows in Fig. 5c and Fig. 5d as well. We have extended the arrows down to the 87 km altitude to show that the occurrence of the bow wave in the OH altitude would be detectable around 0000 UTC when the wave crosses the zenith of the all-sky camera system. However, the bow wave signature can be seen earlier in the bottom of the Na layer in the insets presented in Fig. 5e and Fig. 5f and pointed out by the red-dotted arrows.

The sporadic sodium layer revealed by the ALO lidar scans could have been a consequence of eclipse-triggered sporadic E layers in the lower ionospheric E region. Fig. 9 shows that a sporadic E layer was detected during the eclipse day indeed. Fig. 9 shows the fast enhancement of the electron density associated with the sporadic E near the eclipse totality over the ALO region at 2038 UTC. The Na sporadic layer is visible at around 98 km altitude in the lidar Na density about the same time. Observe in Fig. 9 the virtual altitude of the E_s around $\sim$100 km.

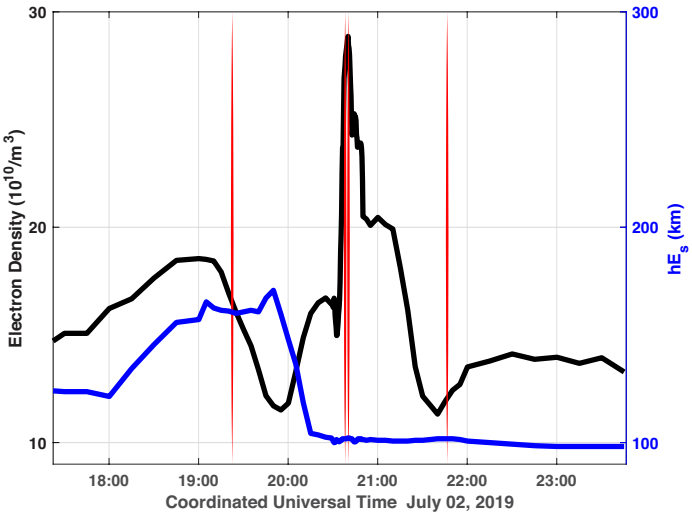

Figure 9. Ionosonde measurements showing the occurrence of a sporadic E layer (E_s) around 100 km during the July 02, 2019 total solar eclipse. The back continuous line represents the E_s electron density and the blue curve the E_s virtual altitude. The vertical red lines indicate the beginning, total obscuration, and the end of the eclipse.

Sporadic E layers are ionization enhancements in the E region at altitudes between 90 and 120 km. The layer densities can be up to an order of magnitude greater than background densities, and the primary ions in the layers are metallic (e.g., Na^+, Fe^+, Mg^+). Neutral metal atoms are created during meteor ablation, and their subsequent ionization via photo-ionization and charge exchange yields the long-lived metallic ions (Schunk & Nagy, 2018). In general, sporadic E layers at mid-latitudes are primarily a result of wind shears. Still, they can also be created by diurnal and semi-diurnal tides and gravity waves (Schunk & Nagy, 2018). The E_s layers are formed when the vertical ion drift changes direction with altitude, and the layers occur at the altitudes where the ion drift converges. In the E region, the zonal neutral wind is primarily responsible for inducing vertical ion drifts, which result from a $u \times B$ dynamo action (u is the zonal wind and B is the geomagnetic field). Hence, a reversal of the zonal neutral wind with altitude will result in ion convergence and divergence regions. The ions accumulate in the convergence regions, but since the molecular ions (NO^+, O_2^+, N_2^+) rapidly recombine, it is the long-lived metallic ions that survive and dominate the sporadic E layers. A strong evidence of zonal wind reversal with altitude is given in Fig. 6d where positive and negative wind shears are seen in the 100–106 km range. Thus, the observed E_s layer was likely caused by the effect of the wind shear supposedly induced directly by eclipse cooling since similar wind shears are not observed in the control days.

Due to gravity waves or tides, sporadic E layers tend to descend to altitudes where recombination of metallic ions is faster. Thus, neutralized metallic ions such as Na^+ would show in lidar scans as sporadic Na layers as shown in Fig. 5c. Because the descending speed of the Na_s layer is similar to that of the diurnal tide, it is likely the Na_s and the E_s time evolution was controlled by the diurnal tide dynamics. Amaro-Rivera et al. (2021) has presented a detailed analysis showing the dominance of tidal modes over ALO using airglow images and numerical simulations.

Bravo et al. (2020) supports the idea that the sporadic E layer is associated with the eclipse, possibly generated by a gravity wave along the path of totality as pointed out by Chen et al. (2011). On the other hand, they show reservations in the claim that the eclipse generated the sporadic E layer once they have also observed E_s in the days preceding the eclipse. However, we have shown the E_s is likely the product of eclipse–induced wind shears in the lower thermosphere. Bravo et al. (2020) also shows reductions in the E electron concentrations following the eclipse's start since the layer electron concentrations are mainly dependent on the production and loss of ionization (Rishbeth, 1968). This direct dependence of the E density on solar radiation shows similarities to previous eclipses measurements at low latitudes, such as September 23, 1987, reported by Cheng et al. (1992). The same feature is also revealed in the measurements and models for the Great American Eclipse of 2017 by Reinisch et al. (2018).

Didebulidze et al. (2020) have demonstrated numerically the possible formation of multilayered sporadic E by gravity waves propagating into the lower thermosphere in mid-latitudes. Their results corroborate measurements of Chen et al. (2011) focused on studying sporadic E_s layer effects over Wuhan, China (30.4°N, 114.3°E). On the other hand, Pezzopane et al. (2015) showed how the March 20, 2015, partial solar eclipse (45–54% maximum obscuration) influenced sporadic E layers using records of advanced ionospheric sounders in Rome (41.8°N, 12.5°E) and Gibilmanna (37.9°N, 14.0°E), Italy. They show that the E_s critical frequencies did not depend on strong thermal gradients, which were comparable between the previous day and the next day. The E_s layer was always present near the solar eclipse time, both at Rome and Gibilmanna. An analysis of isoheight ionogram plots suggests that traveling ionosphere disturbances due to gravity waves played a significant role in the persisting E_s layer.

Thus, based on our findings, it is reasonable to claim that the electron density increase over the eclipse period generated a sporadic E layer. This is likely the product of the wind shear in the lower thermosphere, causing convergence of electrons to a thin region under the influence of the earth's magnetic field. The sporadic E layer then descends due to a downward drift of the plasma under the influence of the diurnal tide dominant over ALO latitude (Amaro-Rivera et al., 2021). At altitudes <100 km, the Na^+ ions in the E_s layer recombine with free electrons producing neutral Na that would be detected by the Lidar system as a sporadic sodium layer (Na_s) (e.g., Raizada et al., 2015). The sporadic Na layer presents peak density around 2250–2330 UTC at 94 ± 2 km, and a wavelike structure is also seen in the temporal structure of the Na_s. The Na_s shows descending progression in time due to the diurnal tide dynamics present over the night. It is possible that the wavelike structure associated with our fast bow wave was locally generated in the ionosphere, traveling downwards and detected in the OH airglow layer (Fig. 2) at 87 km, but more substantial evidence point out to a bow wave excitation below the MLT. This bow wave also caused variations in the Na_s density earlier at an altitude of 98 km earlier and in the OH brightness near 87 km later.

5 Conclusions

We have shown in this paper several effects of July 2, 2019, total eclipse around the MLT region above the Andes Lidar Observatory in Chile. Among remarkable effects, we highlight the excitation of a fast, bow–shaped gravity wave detected in images of the OH(6,2) nightglow, but not directly affecting neither the mesospheric nightglow emissions nor the thermospheric O(^1D) emission. The signature of this spectacular bow wave is also present clearly in MTM OH(6,2) brightness and rotational temperature and lidar temperate and Na density scans. Other eclipse–induced events include a sporadic E layer detected with a nearby ionosonde and a sporadic Na layer presenting a descending phase likely controlled by the diurnal tide dynamics observed in lidar temperatures. We have also noticed strong shears in horizontal wind evident

30 minutes prior to the eclipse totality over ALO as measured by the new meteor radar system. Finally, TIMED/SABER temperature measurements near the eclipse totality region at 243°E meridian revealed strong cooling and warming (±30%) in the range of 90–105 km at 15–25°S. From the analysis of these events, we have drawn the following conclusion:

1. We were unable to confirm whether the cooling/warming seen in SABER temperatures was directly caused by the eclipse because our lidar shows no temperature variation during the eclipse event. However, SABER measurements were taken far away from ALO.
2. The bow wave shows strong magnitude in images of the OH emission, but not in images of the mesospheric molecular and atomic oxygen nightglow layers. This is explained by the formation of a narrow channel in the MLT around 87 km altitude permitting the horizontal propagation of the wave at the OH layer level but not above.
3. The bow wave was likely generated in the lower atmosphere by the cooling effect of the eclipse around the ozone layer's peak or near the tropospheric water vapor layer. The excitation of the bow wave above the MLT is also a possibility. The wave descending phase feature seen in lidar temperature scans reinforces the hypothesis of excitation below the MLT, although we can not pinpoint the exact location.
4. The sporadic E layer observed by a nearby ionosonde was likely generated by shears seen 30 minutes before the eclipse totality in meteor radar winds. These horizontal wind shears were induced by the eclipse at the bottom side of the ionospheric E region, generating the E_s due to the interaction of the sheared background wind and the local magnetic field.
5. The strong descending phase of the diurnal tide caused Na ions present in the sporadic E layer to descend below 100 km. Na ions were then neutralized at lower altitudes and observed as a sporadic Na layer in lidar density scans.
6. The sporadic Na layer presented a larger magnitude near 94 km at 2315 UTC when it also presented a vertical oscillatory motion of 20–25 minutes likely caused by the bow wave seen in the airglow.
7. Although these events present strong signature in our registers, we were unable to see a direct effect of the eclipse on the MLT, but only its induced variations in regions above or below the 80–100 km range and their coupling with the MLT via atmosphere oscillations.

Acknowledgments

The ALO lidar operation was supported by the National Science Foundation (NSF) grants 1759471 and 1759573. The meteor radar installation was supported by NSF grant 1828589. Support for the operations of the USU MTM and associated OH data analyses was provided by the NSF grant number 1911970. F. Vargas and G. Swenson's work in this paper was partially supported by NSF grant 1903336.

References

Amaro-Rivera, Y., Vargas, F., Huang, T.-Y., & Urbina, J. (2021). Unusual intensity patterns of oh(6,2) and o(1s) airglow driven by long-period waves observed over the andes lidar observatory. *Journal of Geophysical Research: Space Physics*, *126*(2), e2020JA028091. Retrieved from `https://agupubs.onlinelibrary.wiley.com/doi/abs/10.1029/2020JA028091` (e2020JA028091 2020JA028091) doi: https://doi.org/10.1029/2020JA028091

Beer, T. (1973). Supersonic generation of atmospheric waves. *Nature*, *242, 34*. doi: 10.1038/242034a0

Beer, T. (1978). On atmospheric wave generation by the terminator. *Planetary and Space Science*, *26*(2), 185 - 188.

Beer, T., & May, A. (1972). Atmospheric gravity waves to be expected from the solar eclipse of June 30, 1973. *Nature*, *240*(5375), 30–32. doi: 10.1038/240030a0

Bravo, M., Martínez-Ledesma, M., Foppiano, A., Urra, B., Ovalle, E., Villalobos, C., ... Stepanova, M. (2020). First report of an eclipse from chilean ionosonde observations: Comparison with total electron content estimations and the modeled maximum electron concentration and its height. *Journal of Geophysical Research: Space Physics*, *125*(9), e2020JA027923. doi: https://doi.org/10.1029/2020JA027923

Chen, G., Zhao, Z., Zhang, Y., Yang, G., Zhou, C., & Huang, S. (2011). Gravity waves and spread Es observed during the solar eclipse of 22 July 2009. *Journal of Geophysical Research*, *116*, 09314. doi: 10.1029/2011JA016720

Cheng, K., Huang, Y.-N., & Chen, S.-W. (1992). Ionospheric effects of the solar eclipse of September 23, 1987, around the equatorial anomaly crest region. *Journal of Geophysical Research: Space Physics*, *97*(A1), 103-111. Retrieved from `https://agupubs.onlinelibrary.wiley.com/doi/abs/10.1029/91JA02409` doi: https://doi.org/10.1029/91JA02409

Chimonas, G. (1974). Internal gravity-wave motions induced in the Earth's atmosphere by a solar eclipse. In *The upper atmosphere in motion* (pp. 708–714). Washington, DC: American Geophysical Union (AGU. doi: 10.1029/GM018p0708

Chimonas, G., & Hines, C. (1970b). Atmospheric gravity waves induced by a solar eclipse. *Journal of Geophysical Research*, *75*(4), 875–875. doi: 10.1029/JA075i004p00875

Chimonas, G., & Hines, C. O. (1970a). Atmospheric gravity waves induced by a solar eclipse. *Journal of Geophysical Research (1896-1977)*, *75*(4), 875-875.

Didebulidze, G. G., Dalakishvili, G., & Todua, M. (2020). Formation of multilayered sporadic E under an influence of atmospheric gravity waves (AGWs). *Atmosphere*, *11*(6), 653. doi: 10.3390/atmos11060653

Eckermann, S. D., Broutman, D., Stollberg, M. T., Ma, J., McCormack, J. P., & Hogan, T. F. (2007). Atmospheric effects of the total solar eclipse of 4 December 2002 simulated with a high-altitude global model. *Journal of Geophysical Research: Atmospheres*, *112*(D14).

Eisenbeis, J., Occhipinti, G., Astafyeva, E., & Rolland, L. (2019). Short- and long-wavelength tids generated by the great american eclipse of 21 August 2017. *Journal of Geophysical Research: Space Physics*, *124*, 9486–9493. doi: 10.1029/2019JA026919

Fritts, D. C., Janches, D., Hocking, W. K., Mitchell, N. J., & Taylor, M. J. (2012). Assessment of gravity wave momentum flux measurement capabilities by meteor radars having different transmitter power and antenna configurations. *Journal of Geophysical Research: Atmospheres*, *117*(D10). Retrieved from `https://agupubs.onlinelibrary.wiley.com/doi/abs/10.1029/2011JD017174` doi: https://doi.org/10.1029/2011JD017174

Goncharenko, L. P., Erickson, P. J., Zhang, S.-R., Galkin, I., Coster, A. J., & Jonah, O. F. (2018). Ionospheric response to the solar eclipse of 21 August 2017 in millstone hill (42n) observations. *Geophysical Research Letters*, *45*(10), 4601-4609. Retrieved from `https://agupubs.onlinelibrary.wiley.com/doi/abs/10.1029/2018GL077334` doi: https://doi.org/10.1029/2018GL077334

Harding, B. J., Drob, D. P., Buriti, R. A., & Makela, J. J. (2018). Nightside detection of a large-scale thermospheric wave generated by a solar eclipse. *Geophysical Research Letters*, *45*(8), 3366-3373. doi: https://doi.org/10.1002/2018GL077015

Harrell, S. D., She, C.-Y., Yuan, T., Krueger, D. A., Plane, J., & Slanger, T. (2010). The faraday filter-based spectrometer for observing sodium nightglow and

studying atomic and molecular oxygen associated with the sodium chemistry in the mesopause region. *Journal of Atmospheric and Solar-Terrestrial Physics*, *72*(17), 1260-1269. doi: https://doi.org/10.1016/j.jastp.2010.08.014

Huba, J. D., & Drob, D. (2017). SAMI3 prediction of the impact of the 21 August 2017 total solar eclipse on the ionosphere/plasmasphere system. *Geophysical Research Letters*, *44*(12), 5928-5935. doi: https://doi.org/10.1002/2017GL073549

Krueger, D., She, C.-Y., & Yuan, T. (2015). Retrieving mesopause temperature and line-of-sight wind from full-diurnal-cycle Na Lidar observations. *Appl. Opt*, *54*(32), 9469–9489.

Kumar, K., Maurya, A., Kumar, S., & Singh, R. (2016). Total solar eclipse induced gravity waves in ionosphere as inferred from gps observations over EIA. *Advances in Space Research*, *58*(9), 1755–1762. doi: 10.1016/j.asr.2016.07.019

Le, H., Liu, L., Yue, X., Wan, W., & Ning, B. (2009). Latitudinal dependence of the ionospheric response to solar eclipses. *Journal of Geophysical Research*, *114*, 07308. doi: 10.1029/2009JA014072

Liu, A., Guo, Y., Vargas, F., & Swenson, G. (2016). First measurement of horizontal wind and temperature in the lower thermosphere (105–140 km) with a Na Lidar at Andes Lidar Observatory, geophys. *Res. Lett*, *43*, 2374–2380,. doi: 10.1002/2016GL068461.

Liu, L., Liu, H., Le, H., Chen, Y., Sun, Y.-Y., Ning, B., ... Xiong, J. (2017). Mesospheric temperatures estimated from the meteor radar observations at mohe, china. *Journal of Geophysical Research: Space Physics*, *122*(2), 2249-2259. Retrieved from `https://agupubs.onlinelibrary.wiley.com/doi/abs/10.1002/2016JA023776` doi: https://doi.org/10.1002/2016JA023776

Marsh, D. R., Smith, A. K., Mlynczak, M. G., & Russell III, J. M. (2006). SABER observations of the OH meinel airglow variability near the mesopause. *Journal of Geophysical Research: Space Physics*, *111*(A10).

Meriwether, J. (1984). Ground based measurements of mesospheric temperatures by optical means. *MAP Handbook*, *13*, 1–18.

Mlynczak, M. G. (1997). Energetics of the mesosphere and lower thermosphere and the SABER experiment. *Advances in Space Research*, *20*(6), 1177 - 1183. (Coupling and Energetics in the Stratosphere-Mesosphere-Thermosphere-Ionosphere System) doi: https://doi.org/10.1016/S0273-1177(97)00769-2

Mohanakumar, K., & Sankaranarayanan, D. (1982). Solar eclipse of February 16, 1980 - it's effect on meteorological parameters. *Proceedings of the Indian National Science Academy*, *48A*, 209.

Müller-Wodarg, I., Aylward, A., & Lockwood, M. (1998). Effects of a mid-latitude solar eclipse on the thermosphere and ionosphere—a modelling study. *Geophysical Research Letters*, *25*(20), 3787–3790. doi: 10.1029/1998GL900045

Paulino, I., Figueiredo, C., Rodrigues, F., Buriti, R., Wrasse, C., & Paulino, A. (2020). Atmospheric gravity waves observed in the nightglow following the 21 August 2017 total solar eclipse. *Geophysical Research Letters*, *47*, e2020GL088924.

Pendleton Jr., W., Taylor, M., & Gardner, L. (2000). Terdiurnal oscillations in OH meinel rotational temperatures for fall conditions at northern mid-latitude sites. *Geophysical Research Letters*, *27*(12), 1799–1802.

Pezzopane, M., Pietrella, M., Pignalberi, A., & Tozzia, R. (2015). 20 March 2015 solar eclipse influence on sporadic E layer. *Advances in Space Research*, *56*(10), 2064–2072. doi: 10.1016/j.asr.2015.08.001

Raitt, W., & Clark, D. (1973). Wave-like disturbances in the ionosphere. *Nature*, *243*, 508–509. doi: 10.1038/243508a0

Raizada, S., Brum, C. M., Tepley, C. A., Lautenbach, J., Friedman, J. S., Mathews, J. D., ... Kerr, C. (2015). First simultaneous measurements of na and k thermospheric layers along with tils from arecibo. *Geophysical Research Letters*, *42*(23), 10,106-10,112. Retrieved from `https://`

agupubs.onlinelibrary.wiley.com/doi/abs/10.1002/2015GL066714 doi: https://doi.org/10.1002/2015GL066714

Reinisch, B. W., Dandenault, P. B., Galkin, I. A., Hamel, R., & Richards, P. G. (2018). Investigation of the electron density variation during the 21 August 2017 solar eclipse. *Geophysical Research Letters*, *45*(3), 1253-1261. Retrieved from https://agupubs.onlinelibrary.wiley.com/doi/abs/10.1002/2017GL076572 doi: https://doi.org/10.1002/2017GL076572

Ridley, E., Dickinson, R., Roble, R., & Rees, M. (1984). Thermospheric response to the June 11, 1983, solar eclipse. *Journal of Geophysical Research*, *89*(A9), 7583–7588. doi: 10.1029/JA089iA09p07583

Rishbeth, H. (1968). Solar eclipses and ionospheric theory. *Space Science Reviews*, *8*(4), 543–554. doi: 10.1007/BF00175006

Rishbeth, H., & Garriot, O. (1969). *Introduction to ionospheric physics, 193–199*. New York & London: Academic Press.

Roble, R., Emery, B., & Ridley, E. (1986). Ionospheric and thermospheric response over millstone hill to the May 30, 1984, annular solar eclipse. *Journal of Geophysical Research*, *91*(5), 1661–1670. doi: https://doi.org/5A8748

Russell, J., Mlynczak, M., Gordley, L., Tansock, J., & Esplin, R. (1999). Overview of the SABER experiment and preliminary calibration results. *Proceedings of SPIE - The International Society for Optical Engineering*, *3756*, 277-288.

Salby, M., L, S., Pielke, R., Pielke, R., & Dmowska, R. (1996). *Fundamentals of atmospheric physics*. Elsevier Science. Retrieved from https://books.google.com/books?id=xWQ0G-_UTBoC

Schunk, R., & Nagy, A. (2018). *Ionospheres: Physics, plasma physics, and chemistry*. Cambridge University Press. Retrieved from https://books.google.com/books?id=VU4oswEACAAJ

Smith, J., & Chu, X. (2015). High-efficiency receiver architecture for resonance-fluorescence and doppler lidars. *Appl. Opt*, *54*(11), 3173 – 3184.

Sun, Y., Liu, J., Lin, C., Lin, C., Shen, M., & Chen, C. (2018). Ionospheric bow wave induced by the moon shadow ship over the continent of united states on 21 August 2017. *Geophysical Research Letters*, *45*, 538–544. doi: 10.1002/2017GL075926

Swenson, G., Liu, A., Li, F., & Tang, J. (2003). High frequency atmospheric gravity wave damping in the mesosphere. *Advances in Space Research*, *32*(5), 785 - 793.

Swenson, G. R., & Gardner, C. S. (1998). Analytical models for the responses of the mesospheric OH* and Na layers to atmospheric gravity waves. *Journal of Geophysical Research: Atmospheres*, *103*(D6), 6271-6294.

Taylor, M., Gardner, L., & Pendleton Jr., W. (2001). Long period wave signatures in mesospheric OH meinel (6,2) band intensity and rotational temperature at mid latitudes. *Advances in Space Research*, *27*(6–7).

Vargas, F. (2019). Traveling ionosphere disturbance signatures on ground-based observations of the O(^1D) nightglow inferred from 1-D modeling. *Journal of Geophysical Research: Space Physics*, *124*(11), 9348-9363. doi: 10.1029/2019JA027356

Vargas, F., Fuentes, J., Vega, P., Navarro, L., & Swenson, G. (2020). Probing the analytical cancellation factor of short scale gravity waves using Na lidar and nightglow data from the Andes Lidar Observatory. *Atmosphere*, *11*(12). doi: 10.3390/atmos11121311

Vargas, F., Swenson, G., Liu, A., & Gobbi, D. (2007). O(^1S), OH, and O_2(b) airglow layer perturbations due to AGWs and their implied effects on the atmosphere. *Journal of Geophysical Research: Atmospheres*, *112*(D14).

Yee, J.-H., Cameron, G. E., & Kusnierkiewicz, D. Y. (1999). Overview of TIMED. In A. M. Larar (Ed.), *Optical spectroscopic techniques and instrumentation for atmospheric and space research iii* (Vol. 3756, pp. 244 – 254). SPIE. doi: 10.1117/12.366378

819 Zhang, S.-R., Erickson, P. J., Goncharenko, L. P., Coster, A. J., Rideout, W., & Vier-
820 inen, J. (2017). Ionospheric bow waves and perturbations induced by the 21
821 August 2017 solar eclipse. *Geophysical Research Letters*, *44*(24), 12,067-12,073.
822 Retrieved from `https://agupubs.onlinelibrary.wiley.com/doi/abs/`
823 `10.1002/2017GL076054` doi: https://doi.org/10.1002/2017GL076054